Electronic Supplementary Material (ESI) for Chemical Science.
This journal is © The Royal Society of Chemistry 2020

Exploring the self-assembly of dumbbell-shaped polyoxometalate hybrids, from molecular building units to nanostructured soft materials.

Mireia Segado Centellas, Madeleine Piot, Raphaël Salles, Anna Proust, Ludovic Tortech, Dalil Brouri, Sébastien Hupin, Benjamin Abécassis, David Landy, Carles Bo,* Guillaume Izzet.*

Contents

1. General methods

Figure S0. Initial box setups denoted as PACKED and UNPACKED systems. Only **K_{Sn}[tpy].Co^{III}** and TBA molecules are depicted.

2. Synthesis and characterizations of K_{Sn}[tpy] and D_{Sn}[tpy]

Figure S1. ^{1}H NMR (300 MHz) and ^{31}P (121 MHz, framed inset) spectra of **K_{Sn}[tpy]** in CD_3CN.
Figure S2. ESI mass spectrum of a solution of **K_{Sn}[tpy]** (10 μM) in MeCN. Inset: Comparison of experimental (upper trace) and calculated (lower trace) isotopic distributions for the ions $[PW_{11}O_{39}SnC_{29}H_{18}N_3]^{4-}$ (*m/z* 801), $[PW_{11}O_{39}SnC_{29}H_{18}N_3.TBA]^{3-}$ (*m/z* 1148) and $[PW_{11}O_{39}SnC_{29}H_{18}N_3.TBA_2]^{2-}$ (*m/z* 1844) of **K_{Sn}[tpy]**.
Figure S3. ^{1}H NMR (300 MHz) ^{31}P (121, framed inset) spectra of **D_{Sn}[tpy]** in CD_3CN.
Figure S4. ESI mass spectrum of a solution of **D_{Sn}[tpy]** (10 μM) in MeCN. Inset: Comparison of experimental (upper trace) and calculated (lower trace) isotopic distributions for the ions $[P_2W_{17}O_{61}SnC_{29}H_{18}N_3.TBA_3]^{4-}$ (*m/z* 1354) and $[P_2W_{17}O_{61}SnC_{29}H_{18}N_3.TBA_4]^{3-}$ (*m/z* 1886) of **D_{Sn}[tpy]**.

3. Complexation of 4'-(4-éthynylphényl)-2,2':6',2''-terpyridine with Co ions

Figure S5. ^{1}H NMR (300 MHz) DMSO-*d$_6$* solution containing 4'-(4-éthynylphényl)-2,2':6',2''-terpyridine (2 mM, top) in the presence of 0.5 equiv of $[Co(H_2O)_6](NO_3)_2$ (middle) and after oxidation of the Co(II) with 0.5 equiv $TBABr_3$ (down).

4. Optimized structure of a molecular dumbbell

Figure S6. Spin density (in blue) of the optimized **K_{Sn}[tpy].Co^{II}** system.

5. SAXS analysis of the discrete species

Figure S7. Computed SAXS pattern (CRYSOL) of the optimized structures of **K_{Sn}[tpy].Co^n** (left) and **D_{Sn}[tpy].Co^n** (right): Co^{II} (red), Co^{III} (black).

6. ^{1}H NMR of the aggregates in CD_3CN

Figure S8. ^{1}H NMR (300 MHz) CD_3CN solution containing **K_{Sn}[tpy]** (2 mM, top) in the presence of 0.5 equiv of $[Co(H_2O)_6](NO_3)_2$ (middle) and after oxidation of the Co(II) with 0.5 equiv $TBABr_3$ (down).
Figure S9. ^{1}H NMR (300 MHz) CD_3CN solution containing **D_{Sn}[tpy]** (2 mM, top left) in the presence of 0.5 equiv of $[Co(H_2O)_6](NO_3)_2$ (middle) and after oxidation of the Co(II) with 0.5

equiv $TBABr_3$ (down).

7. SAXS analysis of the aggregates in CD_3CN

Figures S10. Deconvolution of the SAXS curve (intermediate q region) of **K_{Sn}[tpy].Co^{II}** in MeCN with two Gaussian-shaped components.
Figures S11. Deconvolution of the SAXS curve (intermediate q region) of **K_{Sn}[tpy].Co^{III}** in MeCN with two Gaussian-shaped components.
Figures S12. Deconvolution of the SAXS curve (intermediate q region) of **D_{Sn}[tpy].Co^{II}** in MeCN with two Gaussian-shaped components.
Figures S13. Deconvolution of the SAXS curve (intermediate q region) of **D_{Sn}[tpy].Co^{III}** in MeCN with two Gaussian-shaped components.

8. Transmission electron microscopy of the aggregates

Figure S14. TEM micrographs of **K_{Sn}[tpy].Co^{II}** (left) and **K_{Sn}[tpy].Co^{III}** (right) from MeCN solution after deposition on a grid and rincing with MeCN.

9. SAXS of K_{Sn}[tpy].Co^{III} in DMSO/H_2O mixture

Figure S15. SAXS pattern (subtracted from the solvent and the capillary) of **K_{Sn}[tpy].Co^{III}** in a DMSO-d_6-H_2O mixture.

10. Molecular dynamic simulation

Figure S16. Snapshots of water and DMSO solutions.
Figure S17. Selected POM-POM distances (in Å) from an snapshot taken after 50 ns simulation in the PACKED setup in water.
Figure S18. Computed SAXS pattern (CRYSOL) of 6 snapshots of tetramers aggregates obtained in the PACKED setup in water.
Figure S19. Comparison of intermolecular distance distribution functions between TBA molecules for UNPACKED setup in water (black) and DMSO (red).

11. Analysis of the organogels

Figure S20. Thermogravimetric analysis of **D_{Sn}[tpy]** (black) and **D_{Sn}[tpy].Co^{3+}** as ethanol organogel (red) and hydrogel (blue).
Figure S21. Deconvolution of the SAXS curve (intermediate q region) of **K_{Sn}[tpy].Co^{II}** organogels with two Gaussian-shaped components.
Figure S22. Deconvolution of the SAXS curve (intermediate q region) of **K_{Sn}[tpy].Co^{III}** organogels with two Gaussian-shaped components (left: 1st scan; right: 5th scan).
Figure S23. Deconvolution of the SAXS curve (intermediate q region) of **D_{Sn}[tpy].Co^{II}** organogels with two Gaussian-shaped components.
Figure S24. Deconvolution of the SAXS curve (intermediate q region) of **D_{Sn}[tpy].Co^{III}** organogels with two Gaussian-shaped components (left: 1st scan; right: 5th scan).
Figure S25. SAXS curves of the **POM.Co^n** organogels at very low angles: **K_{Sn}[tpy].Co^{III}** (plain blue), **K_{Sn}[tpy].Co^{II}** (plain red), **D_{Sn}[tpy].Co^{III}** (dotted blue) and **D_{Sn}[tpy].Co^{III}** (dotted red). The black bold curve is indicative of a q^{-2} slope.
Figure S26. Evolution of the signal of **D_{Sn}[tpy].Co^{III}** organogels under successive SAXS acquisition, the bold blue and red lines correspond to the first and last scans respectively.

12. References

1. General methods

Triethylamine was dried over CaH_2 and freshly distilled under argon before use. Dimethylformamide was purchased stored under argon over molecular sieve. Other solvents and reagents were obtained from commercial sources and used as received. Reactions, unless otherwise mentionned, were carried out under dry argon by using Schlenk-tube techniques. **K_{Sn}[I]**,[1] **D_{Sn}[I]**,[2] $[Pd(PPh_3)_2Cl_2]$[3] and 4′-(4-Ethynylphenyl)-2,2′:6′,2″-terpyridine[4] were synthesized according to literature procedures. The ^1H (300.3 MHz), $\{^1H\}$ ^{31}P (121.5 MHz) NMR spectra were obtained at room temperature in 5 mm o.d. tubes on a Bruker AvanceII 300 spectrometer equipped with a QNP probehead. IR spectra were recorded from KBr pellets on a Jasco FT/IR 4100 spectrometer

High resolution ESI-MS experiments were performed on 10 µM solutions of **K_{Sn}[tpy]** or **D_{Sn}[tpy]** in MeCN using a Synapt G2 (Waters Corp., Manchester, UK) hybrid quadrupole/time of flight HDMS instrument equipped with an ESI source. These 10 µM solutions were obtained from 1 mM solutions which were diluted a few minutes prior to the analysis. MassLynx 4.1 software (Waters, Manchester, UK) was used for the spectra acquisition and treatment. The sample solutions were infused into the source with a syringe pump (Cole-Palmer, Vernon Hills, Illinois, USA) set at a flow-rate of 3 $\mu L.min^{-1}$. MS experiments were acquired over a range of 50 to 2000 *m/z* in the negative ion mode (1 s scan time and 0.024 s interscan delay) in either 'V' resolution mode (resolution 20 000 FWHM). The *m/z* values in recorded spectra were first externally calibrated using sodium formate. The ESI source parameters were set as followed: capillary voltage; 2 kV, sample cone voltage; 10 V, extraction cone voltage; 2 V, source temperature; 90 °C, desolvation temperature, 250 °C; nitrogen cone gas flow, 0 $L.h^{-1}$ and nitrogen desolvation gas flow, 500 $L.h^{-1}$. The resulting mass spectrum confirmed the presence of the species and mostly show peaks that correspond to the hybrid POM **K_{Sn}[tpy]** or **D_{Sn}[tpy]**, with various state charge depending of the number of counterions attached (Figures S2 and S4). Relative quantification of the species present in the solution from this mass spectrum is delicate because ions appears with several charge states that all have different response factors so that the relative intensities cannot be considered directly proportional to their relative quantities in solution. The last minute dilution and the instrumental parameters (*electrospray* ionization and ion transmission), although chosen to minimize any dissociation, may also be responsible for the minor formation of the additional ions fragments that were not observed with others analytical technique.

Elemental analyses were performed at the Institut de Chimie des Substances Naturelles, Gif sur Yvette, France.

Isothermal titration calorimetry studies were realized with a VP-ITC calorimeter (MicroCal Inc., USA). Titration experiments were performed at 25 °C for each system, with degassed DMSO solutions. The cell (V_0 = 1425.3 µL) and syringe were filled respectively with a ligand solution (**K_{Sn}[tpy]**, **D_{Sn}[tpy]** or 4'-(4-Ethynylphenyl)-2,2':6',2"-terpyridine) and a $[Co(H_2O)_6](NO_3)_2$ solution. After addition of an initial aliquot of 1 µL, 60 aliquots of 4 µL were delivered over 8 s for each injection, (respectively 1.6 µL over 3.2 s in the case of **D_{Sn}[tpy]**). The agitation speed was set to 350 rpm. The time interval between two consecutive injections was 1000 s, which proved to be sufficient for a complete return to baseline. The resulting heat flow was recorded as a function of time. The peak area following each injection was obtained by integration of the resulting signal. The binding constant and inclusion enthalpy were determined according to the sequential binding site model implemented in the MicroCal Origin software.

Thermogravimetric analyses (TGA) experiments were performed under N_2 flow up to 500 °C, with a heating rate of 10 K/min.

The small-angle X-ray scattering data were acquired on the SWING beamline at synchrotron SOLEIL (Saint Aubin, France). The nanocrystal dispersions were loaded in glass capillaries with an outside diameter between 1 and 1.5 mm and glass walls of 0.01 mm (WJM-Glas, Germany). The energy of the X-ray beam was 12 keV. The scattered X-rays were detected using an EIGER 4 M detector situated at 6.231 or 0.517 m distance from the sample. Ten images were taken with a typical acquisition time of 250 ms and were averaged to increase the signal-to-noise ratio. The SAXS intensity was normalized using beamline-specific procedures and radially averaged using FOXTROT 3.4.1. Deconvolution of the SAXS curves using Gaussian-shaped components was performed on SAXS curves after subtraction with a straight line.

TEM was carried out at the Plateforme de l'Institut des Matériaux de Paris Centre, Sorbonne Université, using a JEM 2011 LaB6 Jeol electron microscope operating at a 200 kV accelerating voltage with a 1.8 Å resolution.

Computational methods

Electronic structure studies and optimization of the geometry of **K$_{Sn}$[tpy].Co^{II}**, **K$_{Sn}$[tpy].Co^{III}**, **D$_{Sn}$[tpy].Co^{II}** and **D$_{Sn}$[tpy].Co^{III}** were carried out using Density Functional Theory (DFT) based methods as implemented in the ADF2016 program.[5] We used the GGA functional BP86,[6] slater type triple-zeta plus polarization basis set, and included solvent effects of DMSO and water implicitly by the COSMO model,[7] and relativistic effects through the relativistic scalar ZORA approach.[8-9] Then, we ran classical molecular dynamics (MD) simulations on solutions of **K$_{Sn}$[tpy].Co^{III}**. We considered four molecules of **K$_{Sn}$[tpy].Co^{III}** in a cubic box of 150x150x150Å. This dimension fulfils the experimental concentration of 1 mM. Two setups were built: one with randomly distributed **K$_{Sn}$[tpy].Co^{III}** units, which we called UNPACKED, and another with a fully organized tetramer of **K$_{Sn}$[tpy].Co^{III}** units, called PACKED (see Figure S0). The box is neutralised with the corresponding 20 TBA counter-cations and filled with ca. 10^5 water molecules, or with $2.6\cdot10^3$ DMSO molecules. The GROMACS 5.0.2 program package was used,[10] all simulations were conducted at 300K under periodic boundary conditions. The temperature was monitored by coupling the system to a weakly-coupling Berendsen thermostat,[11] with a time constant of 0.1 picoseconds (ps). In the NPT simulations, in the last runs, the pressure was coupled to a Parrinello-Rahman barostat[12] with a relaxation time of 2 ps. The Verlet leapfrog algorithm[13] was used to integrate the equations of motion with a time step of 0.5 femtoseconds (fs).

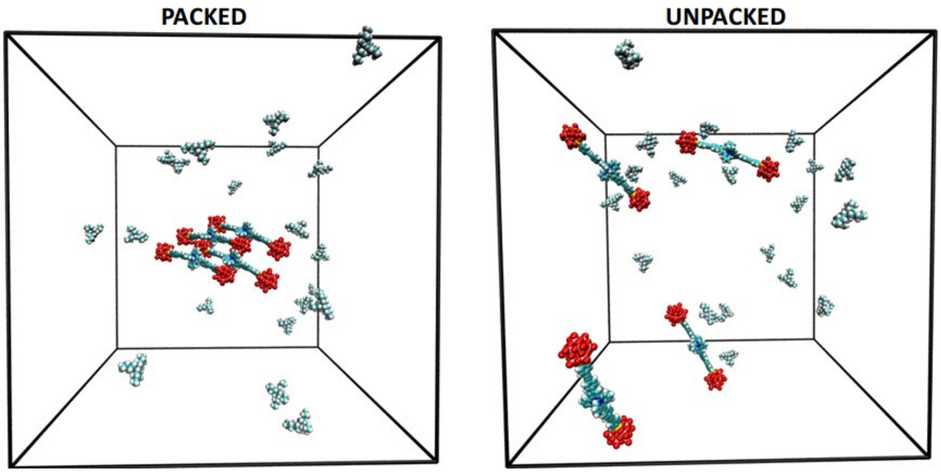

Figure S0. Initial box setups denoted as PACKED and UNPACKED systems. Only **K$_{Sn}$[tpy].Co^{III}** and TBA molecules are depicted.

After energy minimization, we performed three NPT equilibration runs and one final NVT production run. Four nanoseconds (ns) of NPT were performed at 10 ps, and 4 ps barostat time constant, and one last 10 ns NPT equilibration run at 2 ps time constant. Finally we ran a 30 ns NVT production simulation. We applied an atom-based cutoff of 17 Å for non-bonded and coulombic interactions, and correcting for the long-range electrostatics by using the Particle-Particle-Mesh Ewald (PME) summation method.[14] The results of the last 25 ns NVT were analyzed by using Travis trajectory analyser.[15] Data collection was performed every 1 ps. A data set collection of computational results is available in the ioChem-BD repository.

Force field parameters consist of atomic point charges, Lennard-Jones (LJ) parameters and equilibrium-bonded parameters. LJ parameters used here rely in the use of Lorentz−Berthelot combination rules. Water molecules were modelled according to TIP3P[16] and kept rigid during MD simulations by means of SETTLE[17] constraints. The parameters used of DMSO were extracted for the validated for Gromacs CGENFF force field[18] obtained from Virtualchemistry database (http://virtualchemistry.org/). Bonded and non-bonded parameters do not exist for $\mathbf{K_{Sn}[tpy].Co^{III}}$. To generate them, first of all, we took the optimized geometry of $\mathbf{K_{Sn}[tpy].Co^{III}}$ at the DFT level. Then, for the polyoxometalate part, $\mathbf{K_{Sn}}$, we imposed harmonic potential with strong distance constraint based on a very high force constant between every single atom pair within the molecule; in other words, every single atom in $\mathbf{K_{Sn}}$ is constrained to remain within a fixed distance from every other atom in the same molecule, resulting in rigid compact structure, preserving the original optimized input geometry of POM, in an equivalent manner as in previous MD studies on polyoxometalates.[19] For the organic chain part, the parameters for **[tpy]** were generated with *parachem* and taken from the CHARMM general force field (CGenFF). Thus [tpy] part is not considered rigid, and its free to move bonds, angles and dihedrals. In addition we impose an harmonic potential with strong distance and dihedral constraints between $\mathbf{K_{Sn}}$ and **[tpy],** and between Co^{3+} and the six nitrogen atoms of the two [tpy] units coordinated to Co^{3+}, thus preserving in this manner the optimized DFT octahedral structure. LJ parameters for Co^{3+} were taken from CHARMM-compatible force field parameters for several corrinoids developed from quantum mechanical calculations.[20] Quadrupolar multipole derived charges for $\mathbf{K_{Sn}[tpy].Co^{III}}$ were generated at the DFT level with of ADF program. TBA force field was generated with parachem and was taken from the CHARMM general force field (CGenFF) force field.

2. Synthesis and characterizations of K$_{\mathrm{Sn}}$[tpy] and D$_{\mathrm{Sn}}$[tpy]

Synthesis of K$_{\mathrm{Sn}}$[tpy].

A mixture of **K$_{\mathrm{Sn}}$[I]** (300 mg, 0.076 mmol), 4’-(4-éthynylphényl)-2,2’:6’,2’’-terpyridine (51 mg, 0.153 mmol, 2 equiv), CuI (2.3 mg, 0.012 mmol, 0.16 equiv) and $[PdCl_2(PPh_3)_2]$ (6.4 mg, 9.1×10^{-3} mmol, 0.12 equiv) in 4 mL of dry DMF was prepared in a Schlenk tube under Ar atmosphere. After careful degassing with argon for 10 minutes, freshly distilled TEA (200 µL, 1.43 mmol, 19 equiv) was added. The mixture was stirred overnight at room temperature. Upon completion of the reaction (monitored by ^{1}H NMR), the product was then precipitated by the addition of an excess of diethyl ether. The residue was then redisolved in the minimum amont of DMF and diluted into 30 mL of DCM containing TBABr (500 mg, 1.55 mmol, 20 equiv). Some insoluble impurities were discarded and the solution was then concentrated to ca. 5 mL and precipitated upon the addition of an excess of ethanol. The almost colourless solid was then redissolved in ca. 4 mL of MeCN and added to ca. 8 mL of ethyl acetate. A slight brown precipitate was removed from the colorless supernatant that precipitates by the addition of a large excess of diethyl ether, yielding a colourless powder (150 mg, Yield: 48%).

^{1}H NMR (CD_3CN): δ (ppm) = 8.79 ppm (s, 2H), 8.76 (ddd, J = 0.9 Hz, 1.8 Hz, 4.7 Hz, 2H), 8.72 (dt, J_t = 1.0 Hz, J_d = 7.9 Hz, 2H), 7.99 (td, J_d = 1.8 Hz, J_t = 7.7 Hz, 2H), 7.96 (d, J = 8.4 Hz, 2H), 7.79 (d, J = 8.4 Hz, 2H), 7.77 (d, J_{HH} = 8.1 Hz, J_{SnH} = 88 Hz, 2H), 7.69 (d+dd, J_{HH} = 8.1 Hz, J_{SnH} = 40Hz, 2H), 7.47 (ddd, J = 1.0 Hz, 4.7 Hz, 7.5 Hz, 2H), 3.12 (m, 32H), 1.63 (m, 32H), 1.39 (h, J = 7.3 Hz, 32H), 0.99 (t, J = 7.3 Hz, 48H). ^{31}P (CD_3CN): δ (ppm) -10.66 (s+d, J_{SnP} = 24.0 Hz). IR (KBr, cm^{-1}): ν 2960 (s), 2935 (s), 2873 (s), 2233 (s), 1629 (l), 1483 (s), 1474 (s), 1381 (l), 1348 (s), 1069 (s), 962 (s), 885 (s), 811 (s), 711 (l), 662 (l), 514 (m), 381 (s). Elemental analysis for $PW_{11}SnO_{39}C_{29}H_{18}N_3.C_{64}H_{144}N_4$ (%): calcd C 26.76; H 3.91; N 2.35; found 27.08; H 4.11; N 2.23.

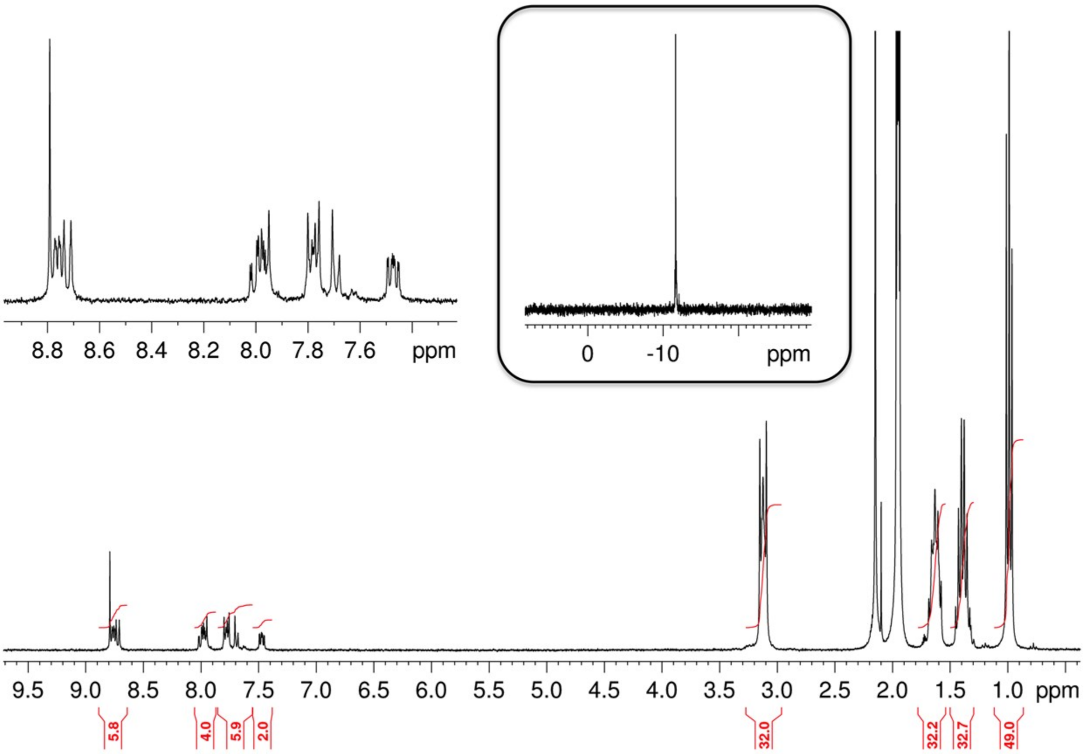

Figure S1. ^{1}H NMR (300 MHz) and ^{31}P (121 MHz, framed inset) spectra of **K$_{\mathrm{Sn}}$[tpy]** in CD_3CN.

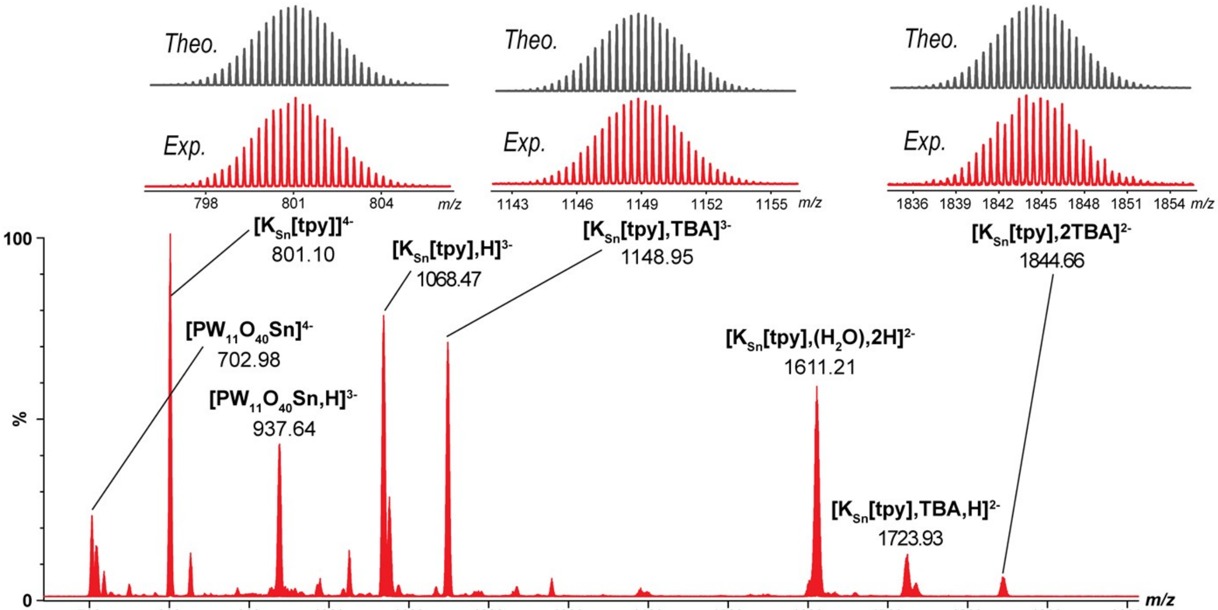

Figure S2. ESI mass spectrum of a solution of **K$_{Sn}$[tpy]** (10 μM) in MeCN. Inset: Comparison of experimental (upper trace) and calculated (lower trace) isotopic distributions for the ions $[PW_{11}O_{39}SnC_{29}H_{18}N_3]^{4-}$ (*m/z* 801), $[PW_{11}O_{39}SnC_{29}H_{18}N_3.TBA]^{3-}$ (*m/z* 1148) and $[PW_{11}O_{39}SnC_{29}H_{18}N_3.TBA_2]^{2-}$ (*m/z* 1844) of **K$_{Sn}$[tpy]**.

Synthesis of $\mathbf{D_{Sn}[tpy]}$

A mixture of $\mathbf{D_{Sn}[I]}$ (200 mg, 0.032 mmol), 4'-(4-éthynylphényl)-2,2':6',2''-terpyridine (21 mg, 0.064 mmol, 2 equiv), CuI (1.0 mg, 5.1×10^{-3} mmol, 0.16 equiv) and $[PdCl_2(PPh_3)_2]$ (2.7 mg, 3.8×10^{-3} mmol, 0.12 equiv) in 4 mL of dry DMF was prepared in a Schlenk tube under Ar atmosphere. After careful degassing with argon for 10 minutes, freshly distilled TEA (134 µL, 0.96 mmol, 30 equiv) was added. The mixture was stirred overnight at room temperature. Upon completion of the reaction (monitored by ^{1}H NMR), the product was then precipitated by the addition of an excess of diethyl ether. The residue is then redisolved in the minimum amont of DMF and diluted into 30 mL of DCM containing TBABr (300 mg, 1.24 mmol, 39 equiv). Some insoluble impurities are then discarded, and the solution is washed 4 times with water. The organic layer was collected and concentrated up to *ca.* 5 mL, precipitated as a colourless solid by addition of diethyl ether (122 mg, 59%).δ (ppm) = 8.79 ppm (s, 2H), 8.76 (ddd, J = 1.0 Hz, 1.8 Hz, 4.7 Hz, 2H), 8.72 (dt, J_t = 1.0 Hz, J_d =7.9 Hz, 2H), 7.99 (td, J_d = 1.8 Hz, J_t = 7.7 Hz, 2H), 7.95 (d, J = 8.4 Hz, 2H), 7.79 (d, J = 8.3 Hz, 2H), 7.77 (m, 4H), 7.62 (d, J = 8.0 Hz), 7.47 (ddd, J = 1.0 Hz, 4.7 Hz, 7.5 Hz, 2H), 3.17 (m, 32H), 1.65 (m, 56H), 1.42 (h, J = 7.3 Hz, 56H), 0.99 (t, J = 7.3 Hz, 84H). ^{31}P (CD_3CN): δ (ppm) -10.49 (s+d, J_{SnP} = 31.0 Hz), -13.54 (s). IR (KBr, cm^{-1}): ν 2961 (s), 2932 (m), 2872 (m), 2206 (w), 1633 (w), 1540 (s), 1472 (s), 1383 (m), 1321 (m), 1264 (w), 1195 (s), 1114 (w), 1070 (s), 963 (vs), 886 (s), 813 (vs), 801 (vs), 717 (w), 705 (w), 661 (w), 515 (w), 381 (s). Elemental analysis for $P_2W_{17}SnO_{61}C_{29}H_{18}N_3.C_{112}H_{252}N_7$ (%): calcd C 26.51; H 4.26; N 2.19; found 25.93; H 4.12; N 2.01.

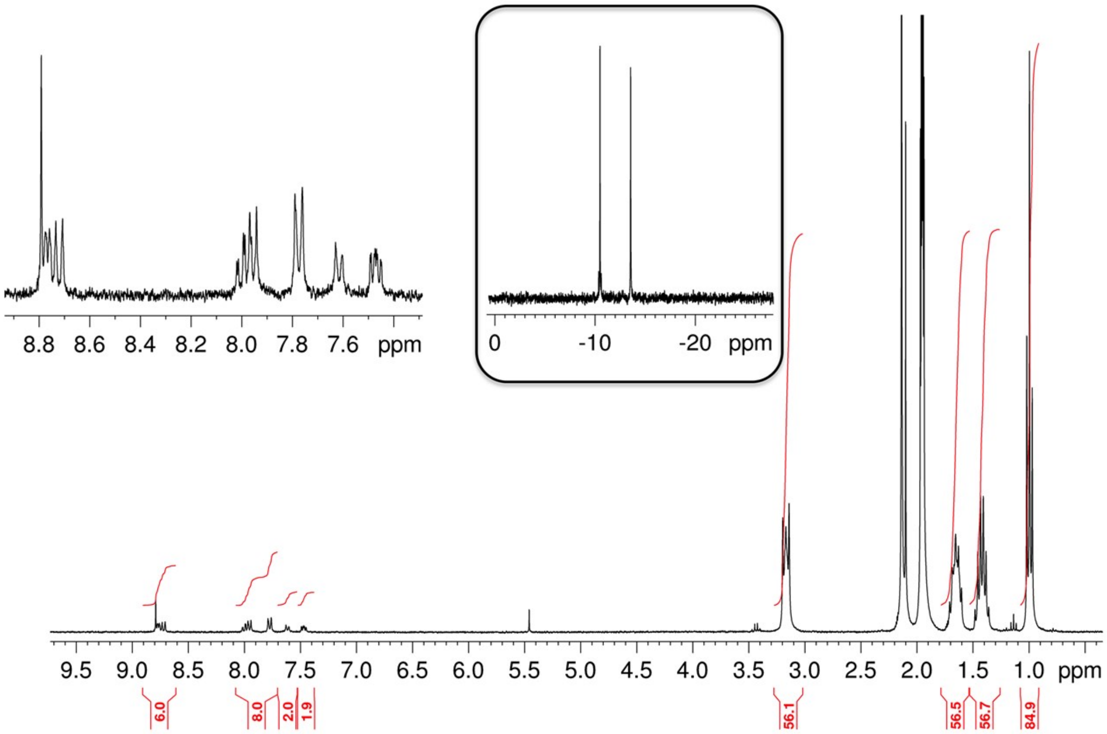

Figure S3. ^{1}H NMR (300 MHz) and ^{31}P (121 MHz, framed inset) spectra of $\mathbf{D_{Sn}[tpy]}$ in CD_3CN.

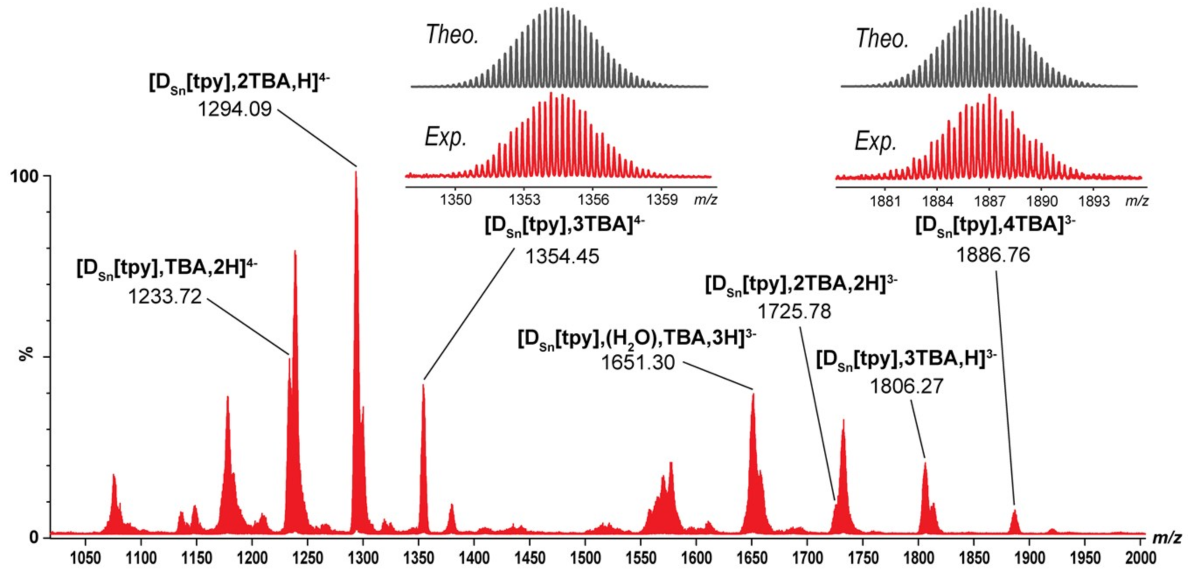

Figure S4. ESI mass spectrum of a solution of **D$_{\mathbf{Sn}}$[tpy]** (10 µM) in MeCN. Inset: Comparison of experimental (upper trace) and calculated (lower trace) isotopic distributions for the ions $[P_2W_{17}O_{61}SnC_{29}H_{18}N_3.TBA_3]^{4-}$ (*m/z* 1354) and $[P_2W_{17}O_{61}SnC_{29}H_{18}N_3.TBA_4]^{3-}$ (*m/z* 1886) of **D$_{\mathbf{Sn}}$[tpy]**.

3. Complexation of 4’-(4-éthynylphényl)-2,2’:6’,2’’-terpyridine with Co ions

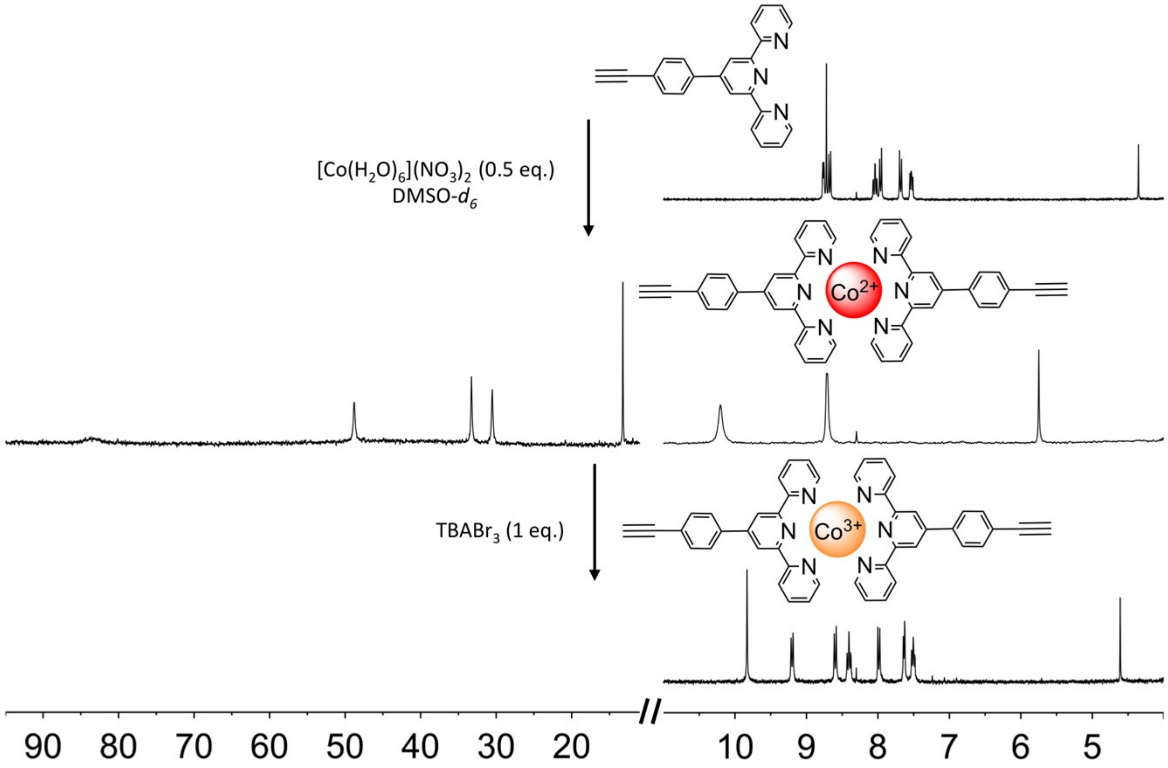

Figure S5. ^{1}H NMR (300 MHz) DMSO-d_6 solution containing 4’-(4-éthynylphényl)-2,2’:6’,2’’-terpyridine (2 mM, top) in the presence of 0.5 equiv of [Co(H$_2$O)$_6$](NO$_3$)$_2$ (middle); after oxidation of the Co(II) with 0.5 equiv TBABr$_3$ (down).

4. Optimized structure of a molecular dumbbell

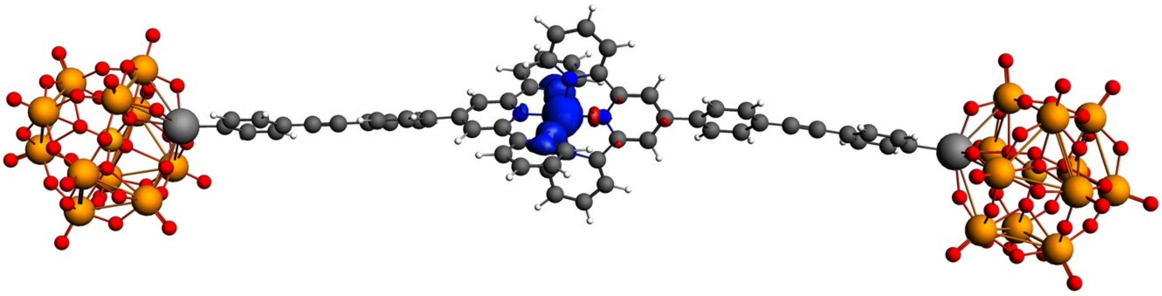

Figure S6. Spin density (in blue) of **$\mathbf{K_{Sn}}$[tpy].Co$^{\mathbf{II}}$** system from DFT geometry optimization.

5. SAXS analysis of the discrete species

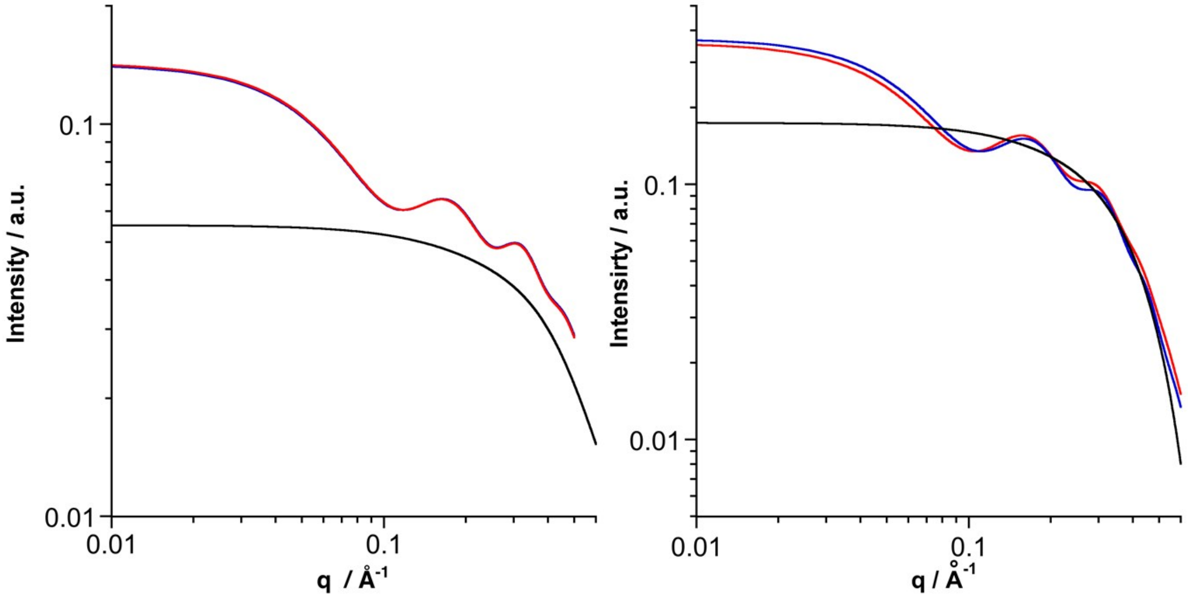

Figure S7. Computed SAXS pattern (CRYSOL) of the optimized structures of **K_{Sn}[tpy]** (black left), **K_{Sn}[tpy].Co^{n}** (red and blue left), **D_{Sn}[tpy]** (black right), and **D_{Sn}[tpy].Co^{n}** (red and blue right): Co^{II} (red), Co^{III} (blue).

6. ^1H NMR of the aggregates in CD_3CN

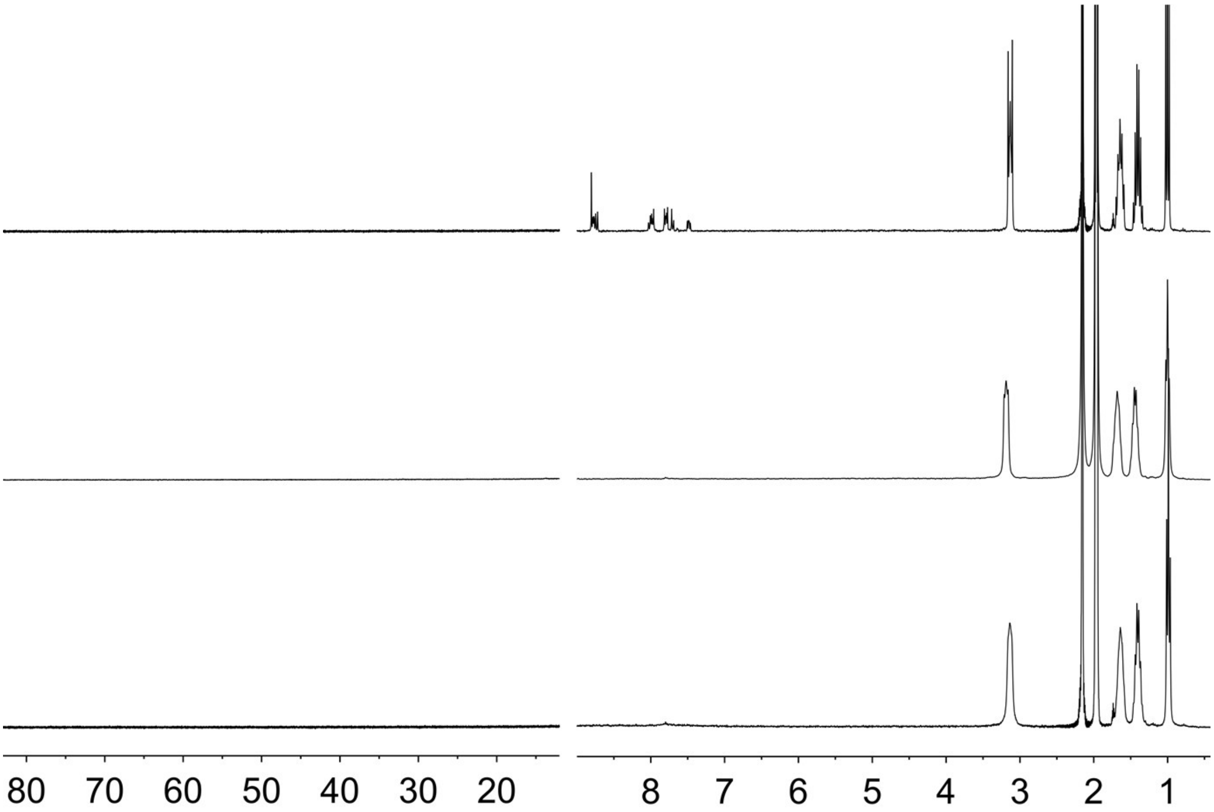

Figure S8. ^1H NMR (300 MHz) CD_3CN solution containing **K_{Sn}[tpy]** (2 mM, top) in the presence of 0.5 equiv of $[Co(H_2O)_6](NO_3)_2$ (middle) and after oxidation of the Co(II) with 0.5 equiv $TBABr_3$ (down).

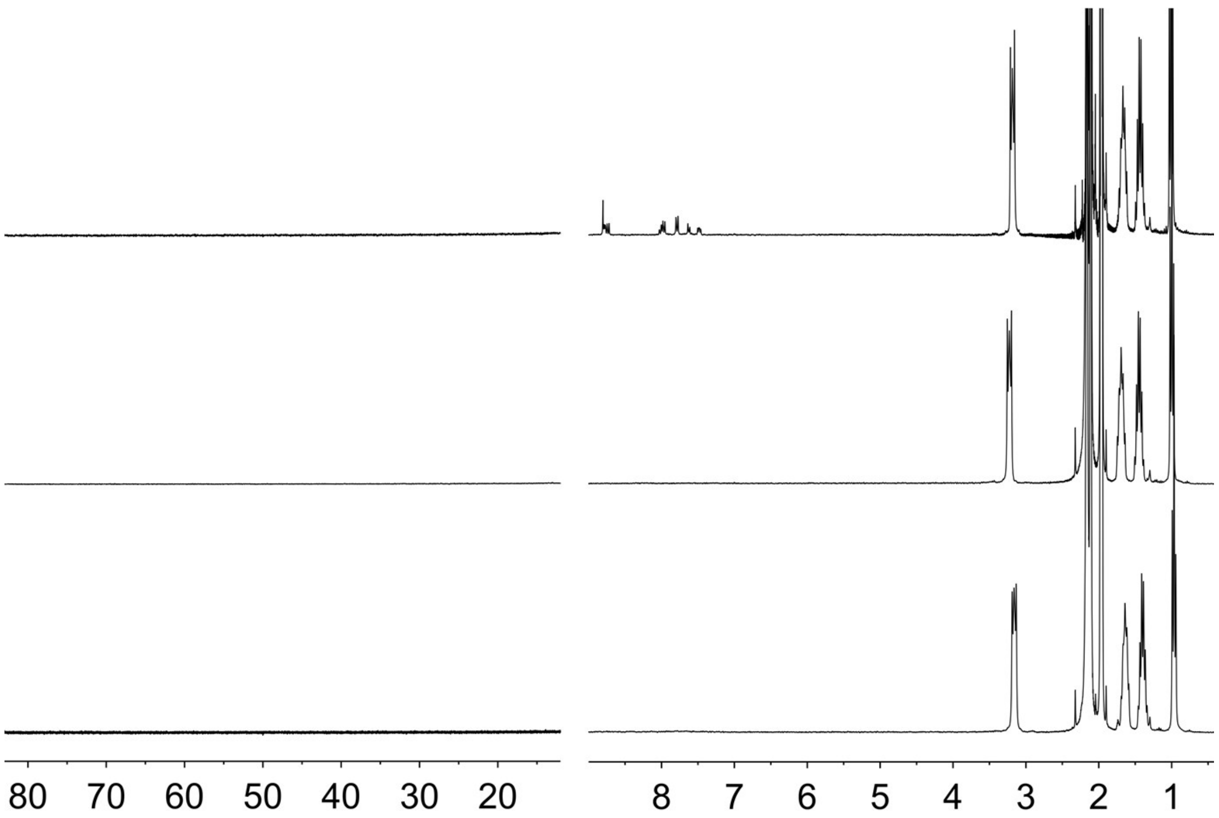

Figure S9. ^1H NMR (300 MHz) CD_3CN solution containing $\mathbf{D_{Sn}[tpy]}$ (2 mM, top) in the presence of 0.5 equiv of $[Co(H_2O)_6](NO_3)_2$ (middle) and after oxidation of the Co(II) with 0.5 equiv $TBABr_3$ (down).

7. SAXS analysis of the aggregates in CD_3CN

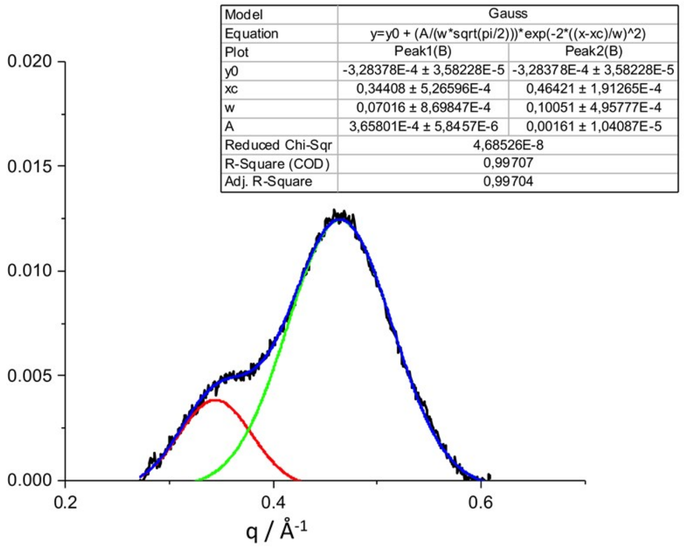

Model	Gauss	
Equation	y=y0 + (A/(w*sqrt(pi/2)))*exp(-2*((x-xc)/w)^2)	
Plot	Peak1(B)	Peak2(B)
y0	-3,28378E-4 ± 3,58228E-5	-3,28378E-4 ± 3,58228E-5
xc	0,34408 ± 5,26596E-4	0,46421 ± 1,91265E-4
w	0,07016 ± 8,69847E-4	0,10051 ± 4,95777E-4
A	3,65801E-4 ± 5,8457E-6	0,00161 ± 1,04087E-5
Reduced Chi-Sqr	4,68526E-8	
R-Square (COD)	0,99707	
Adj. R-Square	0,99704	

Figures S10. Deconvolution of the SAXS curve (intermediate q region) of **K_{Sn}[tpy].Co^{II}** in MeCN with two Gaussian-shaped components.

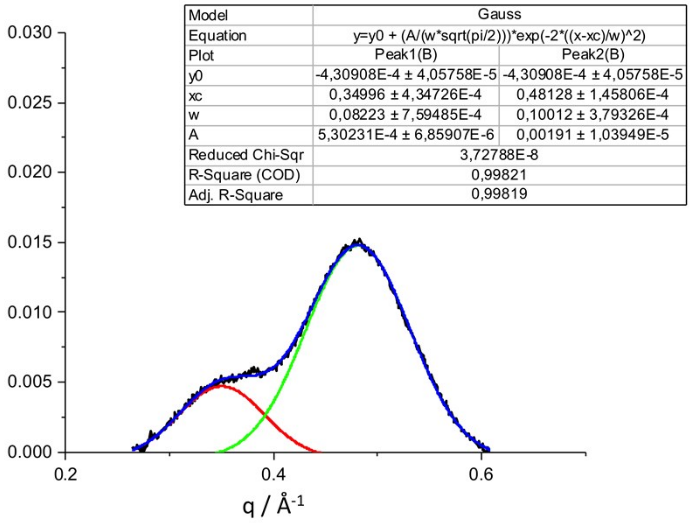

Model	Gauss	
Equation	y=y0 + (A/(w*sqrt(pi/2)))*exp(-2*((x-xc)/w)^2)	
Plot	Peak1(B)	Peak2(B)
y0	-4,30908E-4 ± 4,05758E-5	-4,30908E-4 ± 4,05758E-5
xc	0,34996 ± 4,34726E-4	0,48128 ± 1,45806E-4
w	0,08223 ± 7,59485E-4	0,10012 ± 3,79326E-4
A	5,30231E-4 ± 6,85907E-6	0,00191 ± 1,03949E-5
Reduced Chi-Sqr	3,72788E-8	
R-Square (COD)	0,99821	
Adj. R-Square	0,99819	

Figures S11. Deconvolution of the SAXS curve (intermediate q region) of **K_{Sn}[tpy].Co^{III}** in MeCN with two Gaussian-shaped components.

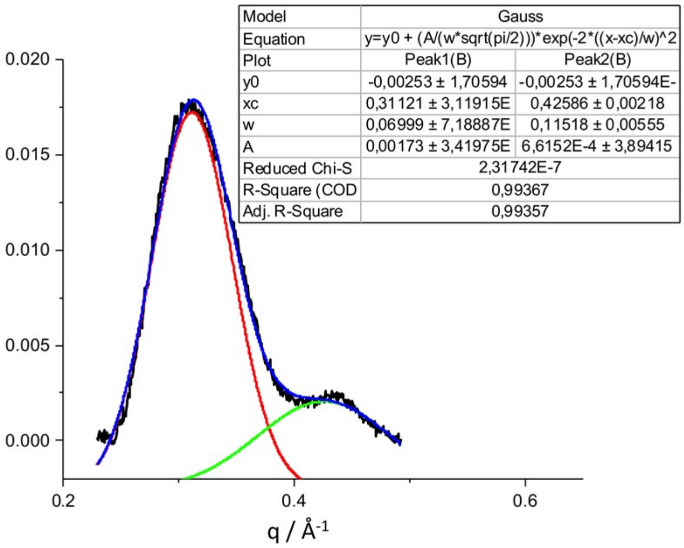

Model	Gauss	
Equation	y=y0 + (A/(w*sqrt(pi/2)))*exp(-2*((x-xc)/w)^2	
Plot	Peak1(B)	Peak2(B)
y0	-0,00253 ± 1,70594	-0,00253 ± 1,70594E-
xc	0,31121 ± 3,11915E	0,42586 ± 0,00218
w	0,06999 ± 7,18887E	0,11518 ± 0,00555
A	0,00173 ± 3,41975E	6,6152E-4 ± 3,89415
Reduced Chi-S	2,31742E-7	
R-Square (COD	0,99367	
Adj. R-Square	0,99357	

Figures S12. Deconvolution of the SAXS curve (intermediate q region) of **D_{Sn}[tpy].Co^{II}** in MeCN with two Gaussian-shaped components.

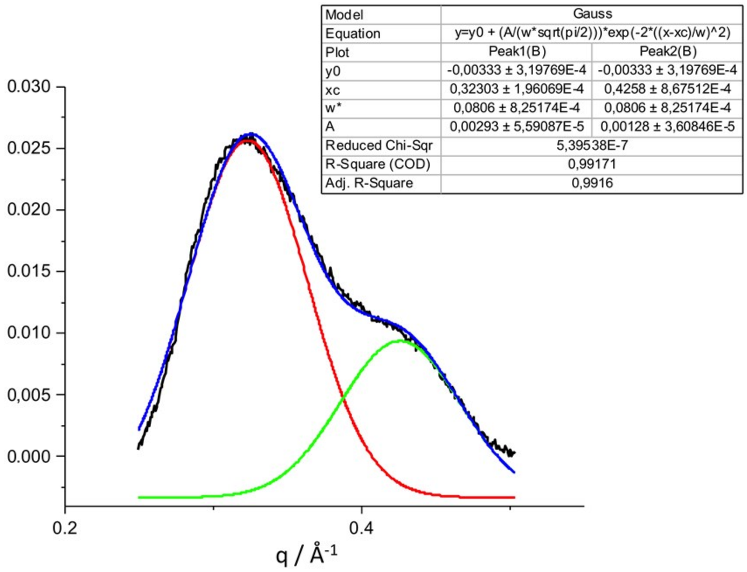

Model	Gauss	
Equation	y=y0 + (A/(w*sqrt(pi/2)))*exp(-2*((x-xc)/w)^2)	
Plot	Peak1(B)	Peak2(B)
y0	-0,00333 ± 3,19769E-4	-0,00333 ± 3,19769E-4
xc	0,32303 ± 1,96069E-4	0,4258 ± 8,67512E-4
w*	0,0806 ± 8,25174E-4	0,0806 ± 8,25174E-4
A	0,00293 ± 5,59087E-5	0,00128 ± 3,60846E-5
Reduced Chi-Sqr	5,39538E-7	
R-Square (COD)	0,99171	
Adj. R-Square	0,9916	

Figures S13. Deconvolution of the SAXS curve (intermediate q region) of **D_{Sn}[tpy].Co^{III}** in MeCN with two Gaussian-shaped components.

8. Transmission electron microscopy of the aggregates

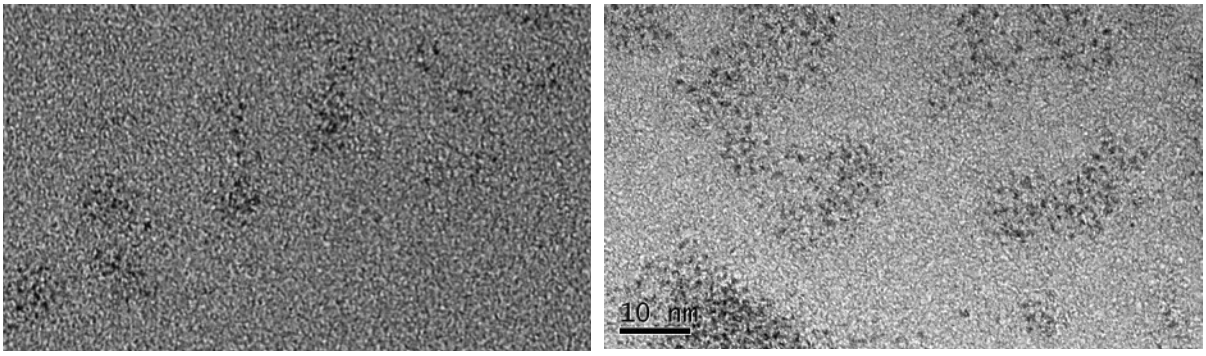

Figure S14. TEM micrographs of $\mathbf{K_{Sn}[tpy].Co^{II}}$ (left) and $\mathbf{K_{Sn}[tpy].Co^{III}}$ (right) from MeCN solution after deposition on a grid and rincing with MeCN.

9. SAXS of $K_{Sn}[tpy].Co^{III}$ in DMSO/H_2O mixture

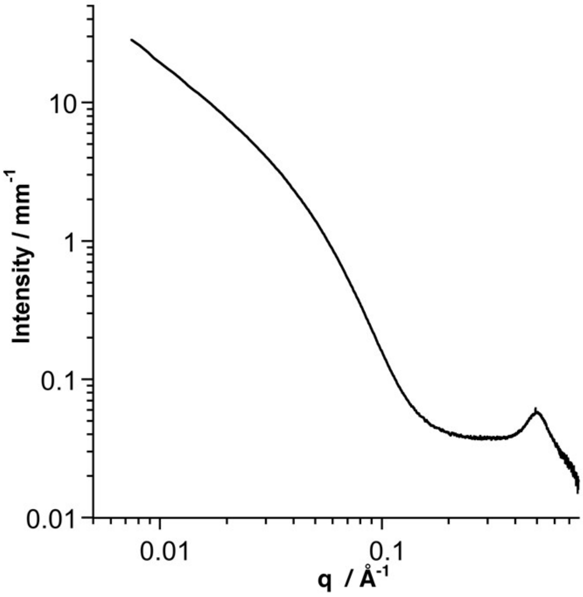

Figure S15. SAXS pattern of $\mathbf{K_{Sn}[tpy].Co^{III}}$ in a DMSO-d_6-H_2O mixture.

10. Molecular dynamics simulations

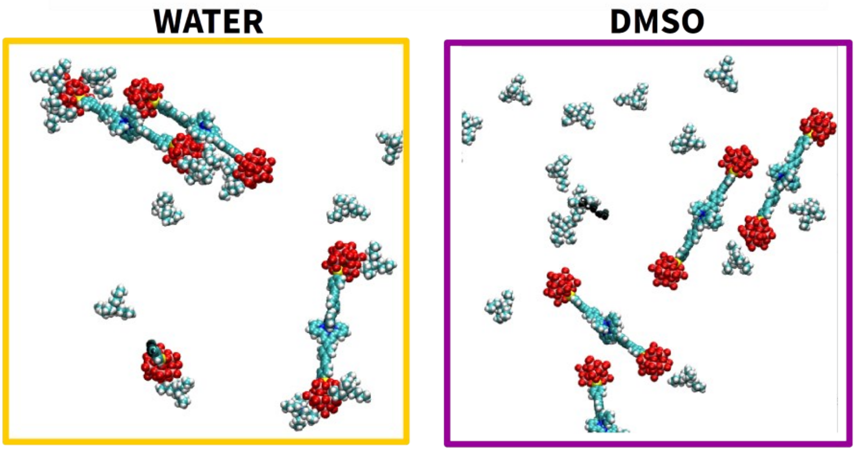

Figure S16. Snapshots of water and DMSO solutions.

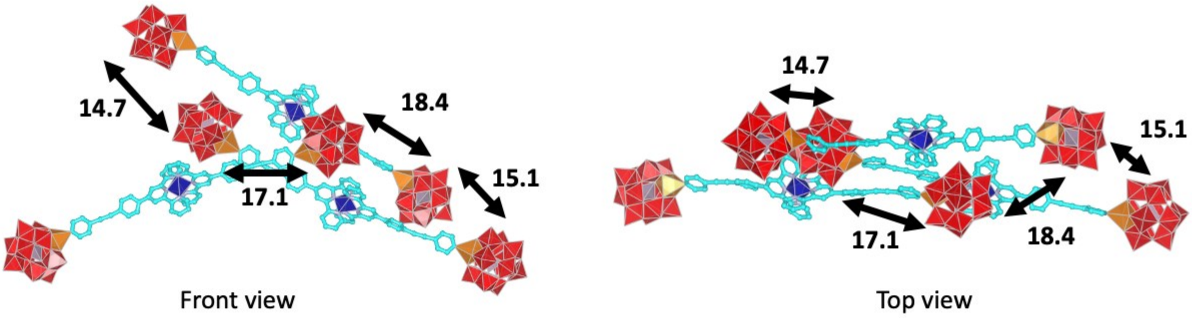

Figure S17. Selected POM-POM distances (in Å) from a snapshot taken after 50 ns simulation in the PACKED setup in water.

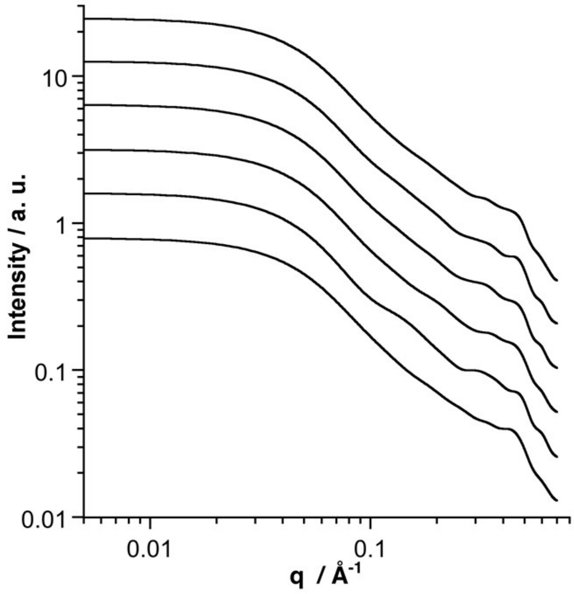

Figure S18. Computed SAXS pattern (CRYSOL) of 6 snapshots of tetramers aggregates obtained in the PACKED setup in water.

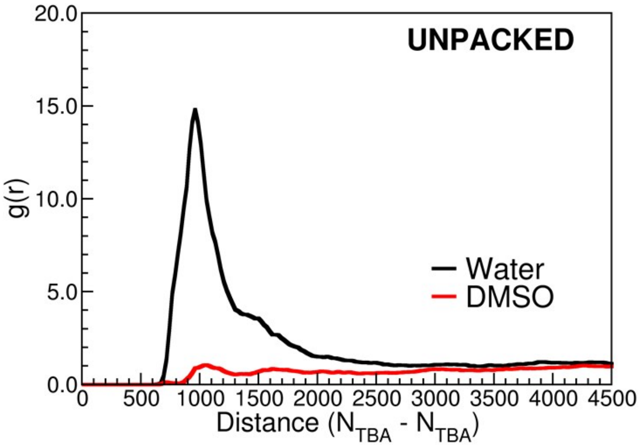

Figure S19. Comparison of intermolecular distance distribution functions between TBA molecules for UNPACKED setup in water (black) and DMSO (red).

11. Analysis of the organogels

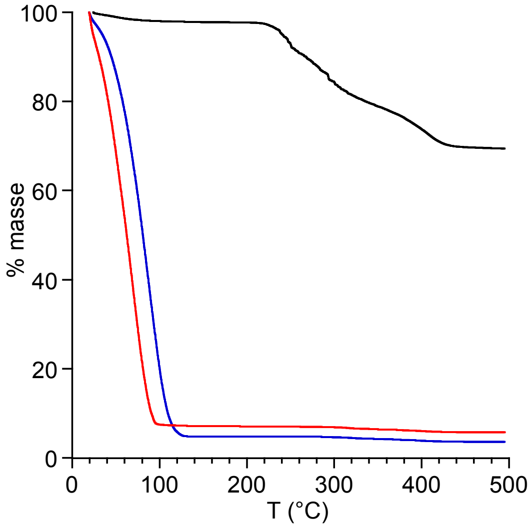

Figure S20. Thermogravimetric analysis of **D_{Sn}[tpy]** (black) and **D_{Sn}[tpy].Co^{3+}** as ethanol organogel (red) and hydrogel (blue).

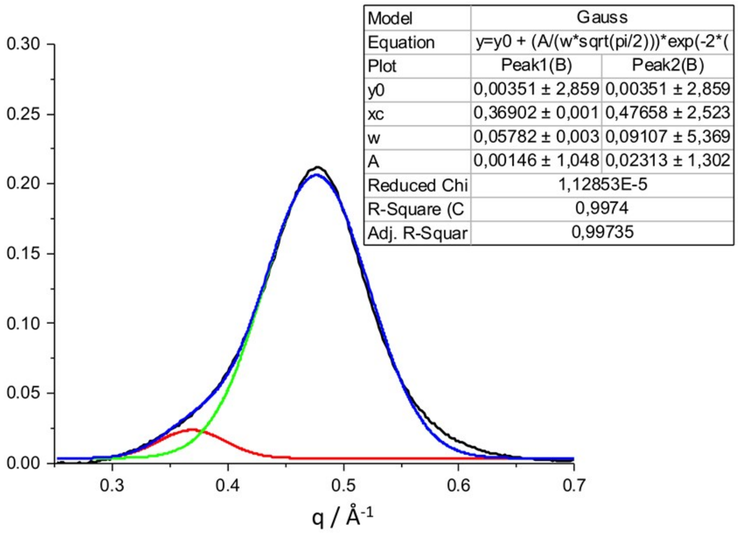

Model	Gauss	
Equation	y=y0 + (A/(w*sqrt(pi/2)))*exp(-2*(	
Plot	Peak1(B)	Peak2(B)
y0	0,00351 ± 2,859	0,00351 ± 2,859
xc	0,36902 ± 0,001	0,47658 ± 2,523
w	0,05782 ± 0,003	0,09107 ± 5,369
A	0,00146 ± 1,048	0,02313 ± 1,302
Reduced Chi	1,12853E-5	
R-Square (C	0,9974	
Adj. R-Squar	0,99735	

Figures S21. Deconvolution of the SAXS curve (intermediate q region) of **K_{Sn}[tpy].Co^{II}** organogels with two Gaussian-shaped components.

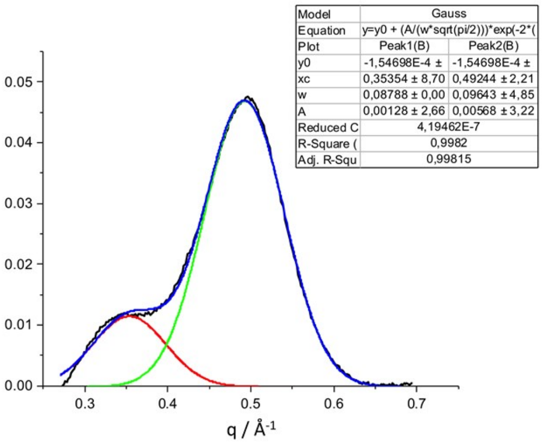

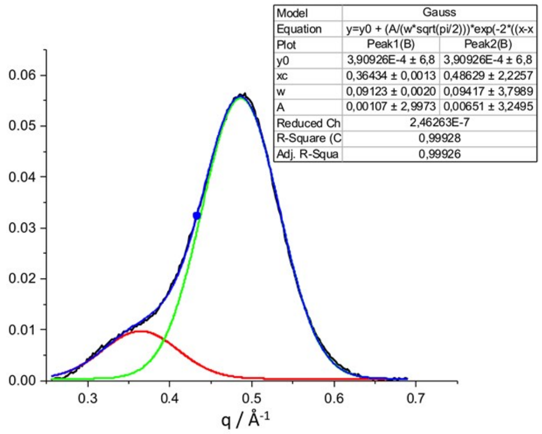

Figures S22. Deconvolution of the SAXS curves (intermediate q region) of **K_{Sn}[tpy].Co^{III}** organogels with two Gaussian-shaped components (left: 1st scan; right: 5th scan).

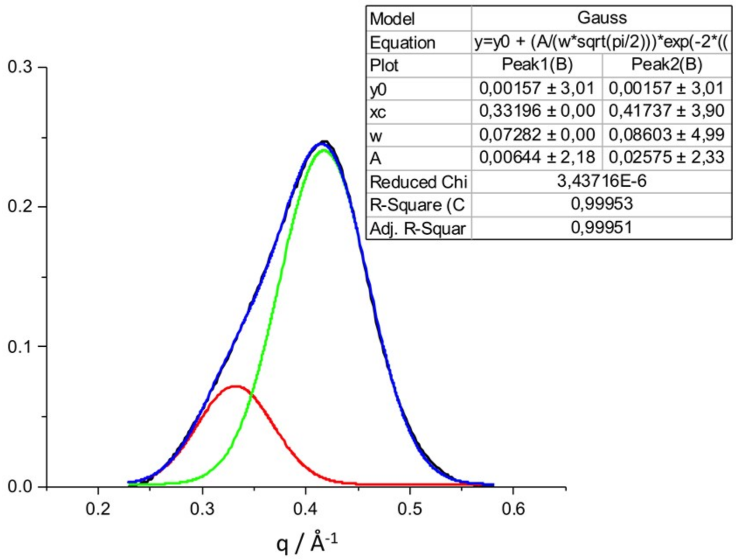

Figures S23. Deconvolution of the SAXS curve (intermediate q region) of **D_{Sn}[tpy].Co^{II}** organogels with two Gaussian-shaped components.

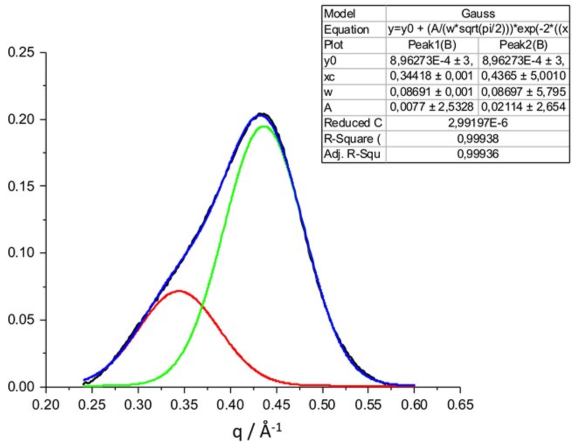

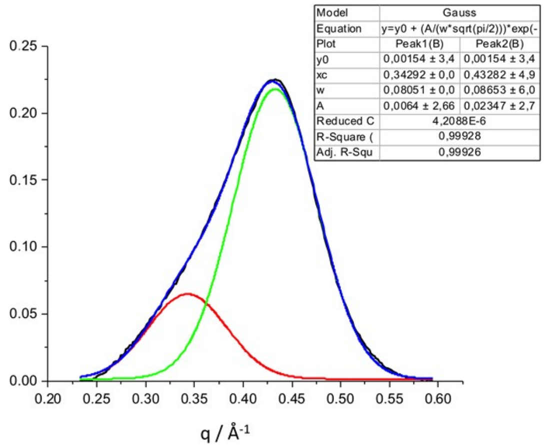

Figures S24. Deconvolution of the SAXS curve (intermediate q region) of **D_{Sn}[tpy].Co^{III}** organogels with two Gaussian-shaped components (left: 1st scan; right: 5th scan).

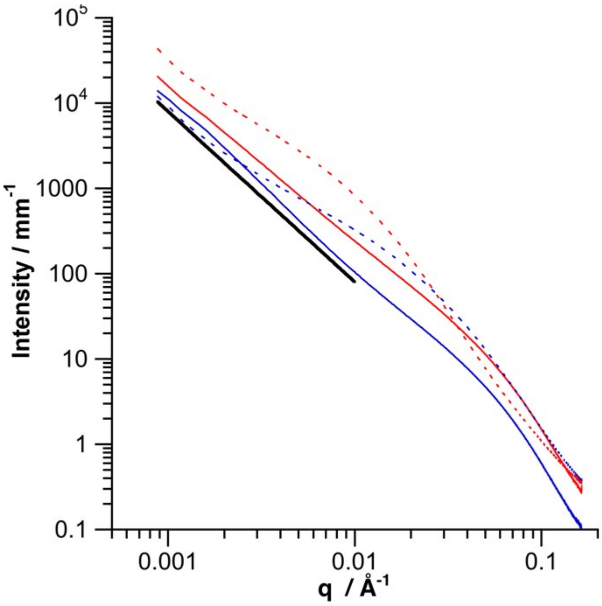

Figure S25. SAXS curves of the **POM.Co^n** organogels at very low angles: **K$_{Sn}$[tpy].Co^{III}** (plain blue), **K$_{Sn}$[tpy].Co^{II}** (plain red), **D$_{Sn}$[tpy].Co^{III}** (dotted blue) and **D$_{Sn}$[tpy].Co^{III}** (dotted red). The black bold curve is indicative of a q^{-2} slope.

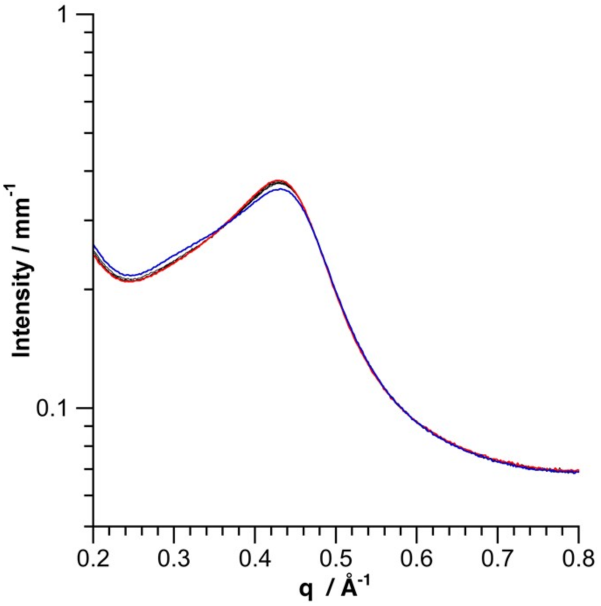

Figure S26. Evolution of the signal of **D$_{Sn}$[tpy].Co^{III}** organogels under successive SAXS acquisition, the bold blue and red lines correspond to the first and last scans respectively.

12. References

1. Matt, B.; Moussa, J.; Chamoreau, L. M.; Afonso, C.; Proust, A.; Amouri, H.; Izzet, G., Elegant Approach to the Synthesis of a Unique Heteroleptic Cyclometalated Iridium(III)-Polyoxometalate Conjugate. *Organometallics* **2012,** *31* (1), 35-38.
2. Rinfray, C.; Renaudineau, S.; Izzet, G.; Proust, A., A covalent polyoxomolybdate-based hybrid with remarkable electron reservoir properties. *Chem. Commun.* **2014,** *50* (62), 8575-8577.
3. Dangles, O.; Guibe, F.; Balavoine, G.; Lavielle, S.; Marquet, A., Selective Cleavage of the Allyl and Allyloxcarbonyl Groups through Palladium-Catalyzed Hydrostannolysis with Tributyltin Hydride - Application to the Selective Protection-Deprotection of Amino-Acid Derivatives and in Peptide-Synthesis. *J. Org. Chem.* **1987,** *52* (22), 4984-4993.
4. Grosshenny, V.; Romero, F. M.; Ziessel, R., Construction of preorganized polytopic ligands via palladium-promoted cross-coupling reactions. *J. Org. Chem.* **1997,** *62* (5), 1491-1500.
5. te Velde, G.; Bickelhaupt, F. M.; Baerends, E. J.; Guerra, C. F.; Van Gisbergen, S. J. A.; Snijders, J. G.; Ziegler, T., Chemistry with ADF. *J. Comput. Chem.* **2001,** *22* (9), 931-967.
6. Perdew, J. P., Density-Functional Approximation for the Correlation-Energy of the Inhomogeneous Electron-Gas. *Physical Review B* **1986,** *33* (12), 8822-8824.
7. Klamt, A., Conductor-Like Screening Model for Real Solvents - a New Approach to the Quantitative Calculation of Solvation Phenomena. *J. Phys. Chem.* **1995,** *99* (7), 2224-2235.
8. vanLenthe, E.; vanLeeuwen, R.; Baerends, E. J.; Snijders, J. G., Relativistic regular two-component Hamiltonians. *Int. J. Quantum Chem.* **1996,** *57* (3), 281-293.
9. Van Lenthe, E.; Baerends, E. J., Optimized slater-type basis sets for the elements 1-118. *J. Comput. Chem.* **2003,** *24* (9), 1142-1156.
10. Abraham, M. J.; Murtola, T.; Schulz, R.; Páll, S.; Smith, J. C.; Hess, B.; Lindahl, E., GROMACS: High performance molecular simulations through multi-level parallelism from laptops to supercomputers. *SoftwareX* **2015,** *1-2*, 19-25.
11. Berendsen, H. J. C.; Postma, J. P. M.; Vangunsteren, W. F.; Dinola, A.; Haak, J. R., Molecular-Dynamics with Coupling to an External Bath. *J. Chem. Phys.* **1984,** *81* (8), 3684-3690.
12. Parrinello, M.; Rahman, A., Crystal-Structure and Pair Potentials - a Molecular-Dynamics Study. *Phys. Rev. Lett.* **1980,** *45* (14), 1196-1199.
13. Hockney, R. W.; Goel, S. P.; Eastwood, J. W., Quiet High-Resolution Computer Models of a Plasma. *J. Comput. Phys.* **1974,** *14* (2), 148-158.
14. Darden, T.; York, D.; Pedersen, L., Particle Mesh Ewald - an N.Log(N) Method for Ewald Sums in Large Systems. *J. Chem. Phys.* **1993,** *98* (12), 10089-10092.
15. Brehm, M.; Kirchner, B., TRAVIS - A Free Analyzer and Visualizer for Monte Carlo and Molecular Dynamics Trajectories. *J. Chem. Inf. Model.* **2011,** *51* (8), 2007-2023.
16. Jorgensen, W. L.; Chandrasekhar, J.; Madura, J. D.; Impey, R. W.; Klein, M. L., Comparison of Simple Potential Functions for Simulating Liquid Water. *J. Chem. Phys.* **1983,** *79* (2), 926-935.
17. Miyamoto, S.; Kollman, P. A., Settle - an Analytical Version of the Shake and Rattle Algorithm for Rigid Water Models. *J. Comput. Chem.* **1992,** *13* (8), 952-962.
18. Vanommeslaeghe, K.; Hatcher, E.; Acharya, C.; Kundu, S.; Zhong, S.; Shim, J.; Darian, E.; Guvench, O.; Lopes, P.; Vorobyov, I.; MacKerell, A. D., CHARMM General Force Field: A Force Field for Drug-Like Molecules Compatible with the CHARMM All-Atom Additive Biological Force Fields. *J. Comput. Chem.* **2010,** *31* (4), 671-690.

19. Lopez, X.; Nieto-Draghi, C.; Bo, C.; Avalos, J. B.; Poblet, J. M., Polyoxometalates in solution: Molecular dynamics simulations on the alpha-PW12O403- keggin anion in aqueous media. *J. Phys. Chem. A* **2005,** *109* (6), 1216-1222.

20. Pavlova, A.; Parks, J. M.; Gumbart, J. C., Development of CHARMM-Compatible Force-Field Parameters for Cobalamin and Related Cofactors from Quantum Mechanical Calculations. *J. Chem. Theory Comput.* **2018,** *14* (2), 784-798.